Available online at www.sciencedirect.com

ScienceDirect

journal homepage: www.elsevier.com/locate/he

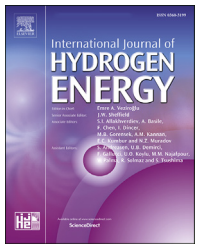

Structural analysis of PdRh/C and PdSn/C and its use as electrocatalysts for ethanol oxidation in alkaline medium

Eric H. Fontes [a,*], *Carlos Eduardo D. Ramos* [a], *Júlio Nandenha* [a], *Ricardo M. Piasentin* [a], *Almir O. Neto* [a], *Richard Landers* [b]

[a] *Instituto de Pesquisas Energéticas e Nucleares, IPEN/CNEN, Centro de Células a Combustível e Hidrogênio, São Paulo, CEP 05508-000, Brazil*

[b] *Universidade Estadual de Campinas, Instituto de Física Gleb Wataghin, Campinas, CEP 13083-859, Brazil*

ARTICLE INFO

Article history:
Received 19 August 2018
Received in revised form
23 October 2018
Accepted 8 November 2018
Available online 1 December 2018

Keywords:
PdSn/C electrocatalyst
PdRh/C electrocatalyst
Ethanol electro-oxidation
DEFC

ABSTRACT

The Pd/C, PdRh(50:50)/C and PdSn(50:50)/C nanomaterials were used as electrocatalysts for ethanol (EtOH) oxidation in Direct Ethanol Fuel Cell (DEFC) in an alkaline medium. This work aims to provide a complete physical characterization of the nanomaterials, elucidate the bifunctional mechanism concerning ethanol oxidation reaction and understand the influence of carbon – metal bonding in the electrochemical activity. These nanomaterials were investigated by X-ray photoelectron spectroscopy (XPS) and revealed that the atomic percentage of the surface is different of those obtained by Energy Dispersive X-ray spectroscopy (EDS). Raman spectroscopy showed a bonding between palladium and carbon atoms which can play a decisive role in the performance of the materials. Attenuated Total Reflectance technique coupled to the Fourier Transform Infrared spectroscopy (ATR-FTIR) made possible to investigate the oxidation products originated by the ethanol oxidation, and all the electrocatalysts showed the presence of acetaldehyde, carbonate ions, acetate and carbon dioxide, suggesting that the mechanism of oxidation is incomplete. Among all the nanomaterials studied, PdSn(50:50)/C showed the best electrochemical and Fuel Cell's results. It is about 33% better than Pd/C. The micrographs obtained by Transmission Electron Microscopy (TEM) revealed some agglomerate regions, but they are consistent with the literature data.

Introduction

Recently, ethanol has shown a variety of applications in technological segments [1]. One of these is the fuel cells. The energy produced by a DEFC is higher when compared to a (DMFC) Direct Methanol Fuel Cell, 8.0 kW $h^{-1}kg^{-1}$ vs 6.0 kW $h^{-1}kg^{-1}$. Besides that, ethanol is less toxic than methanol, it is produced in larger amounts, and it is easier to transport and storage [1,2]. But it is still a challenge to use ethanol in DEFC, mainly due to lower kinetics in acidic medium and it is challenging to cleavage the C-C bond, a necessary requisite to achieve the carbon dioxide production [3].

* *Corresponding author.*
E-mail address: ericfisico@usp.br (E.H. Fontes).
https://doi.org/10.1016/j.ijhydene.2018.11.049

Some studies revealed that OH^- strong adsorption on active sites of ruthenium could improve the (EOR) ethanol oxidation reaction [4], so it is essential to have a reactional medium rich in OH^- species. Recent studies have shown that palladium is a better electrocatalyst in an alkaline medium when it is compared to platinum [1]. Zhang et al., 2011 [5] showed that palladium exhibited almost four times the peak current density of the platinum in cyclic voltammetry experiment. But palladium is expensive, even when compared to platinum. So, it is necessary to reduce the amount of first metal (palladium) and add other types of less expansive metals. In this study, we used two different metals coupled to palladium - tin and rhodium. Tin metals are less noble and less expansive. They can provide a significant amount of oxygenating species, so that the electrocatalytic activity may be due exclusively to the bifunctional mechanism, where the intermediate species can be oxidized in lower potentials [6]. By the other side, rhodium can cleave the C-C bond easier, so the amount of carbon dioxide should be more significant, and the oxidation mechanism will be said to be complete, in which twelve electrons are emitted when one ethanol molecule is completed oxidized. But if the addition of the second metal forms a metallic alloy with palladium, the energy of adsorption with the intermediate species will decrease, and the poisoning effect will also decrease, leading to a better electrocatalytic activity [7]. Maksic' et al., 2016 [8] showed that bimetallic Rh/Pd (poly) prepared by spontaneous deposition of nanoislands of rhodium on polycrystalline palladium, with 50% of rhodium coverage, presented a better performance than bare palladium toward (EOR). They proposed that this improvement was mainly due to the capacity of Rh/Pd oxidize intermediates like carbon monoxide, and, at some level, this capacity led to the formation of carbon dioxide. Other study showed that the addition of rhodium to palladium nanoparticles improved the thermodynamics of methanol oxidation reaction on the catalyst surface [9]. Some works in literature [10] showed that the addition of tin on Pd/C and Pd/MWCNT (Multi-Walled Carbon Nanotube) in alkaline medium, made it possible to oxidize intermediates adsorbed on palladium active sites at lower potentials, and this was explained by the bifunctional mechanism. Besides that [11], could not fully characterize the PdSn/C material, although they have proposed that the mechanism should happen following the bifunctional mechanism. In this context, this work aimed to prepare Pd/C, PdRh(50:50)/C and PdSn(50:50)/C electrocatalysts, in different atomic ratios indicated by the number in parenthesis, by borohydride reduction method. It also aims to perform structural analysis and test them for ethanol electro-oxidation in an alkaline medium through cyclic voltammetry (CV), chronoamperometry and in a DEFC.

Results

Structural characterization: Raman spectroscopy, XPS, EDS-SEM, TEM and XRD

In 2.1, we will present the structural characterization of Pd/C, PdSn(50:50)/C and PdRh(50:50)/C electrocatalysts.

Raman spectroscopy

Fig. 1 shows the Raman spectra of Carbon Vulcan XC72, Pd/C, PdRh(50:50)/C and Rh/C and PdSn(50:50)/C. In supplemental material, S1 shows the curve fitting of the D and G bands of Carbon Vulcan XC72. In S1, at first, it is possible to see two peaks, one in 1315 and the other one in 1595 cm^{-1} related to the D and G bands; these bands are characteristics of carbon structures. However, when these peaks are deconvoluted, there can be seen five different Gaussian functions at 1213.6, 1314.9, 1560.6, 1613 and 1420.6 cm^{-1}. These bands are related to the modes D′, G, D3, D and D4 which are characteristics of carbon black structure [12].

X-ray photoelectron spectroscopy

Figs. 2–4, and in supplemental material S2 and S3, show the XPS spectra of Pd/C, PdRh(50:50)/C, PdSn(50:50)/C electrocatalysts and the oxidation states of these metals as well as the bonds with carbon and oxygen. The curve fitting agrees with the XPS theory and some reports, for instance, Pd3d doublet peak separation obtained was 5.28 eV for Pd/C, and (Moulder, 1992) [13] shows that this separation is 5.25 eV. The ratio area in $Pd3d_{5/2}$ and $Pd3d_{3/2}$, $Sn3d_{5/2}$ and $Sn3d_{3/2}$, $Rh3d_{5/2}$ and $Rh3d_{3/2}$ peaks used in the curve fitting was 1.5, and as it can be seen, these fits match the experimental curves, and it's in accordance with the XPS theory [14]. In Pd/C, it was possible to observe the presence of $Pd3d_{5/2}$ and $Pd3d_{3/2}$ doublet peaks. When curve fitting was made on these peaks, using Gaussian functions [15], it was possible to identify different metal oxidation states, as well as the Pd metallic. Taking the $Pd3d_{5/2}$ as the main peak, we can locate Pd^0 in 335.3 eV, while [13] report this peak at 334.9 eV. So, we can say that Pd^0 is present in Pd/C. It was also possible to identify the presence of PdO in Pd/C. Curve fitting showed the existence of this metal oxide in approximately 337.5 eV, while [15] report this presence in 337.1 eV and [13] in 336.1 eV. It is also interesting to notice the presence of palladium through $Pd3p_{3/2}$ on O1s spectra. But the signal is less intense, so it is not possible to analyze different chemical shifts of palladium in this band. The distance between the Pd3d experimental doublets peaks center is about 5.28 eV, while [13] report this distance as 5.25 eV, showing a good agreement between the results and the literature. In PdRh(50:50)/C, it was possible to identify the Rh3d doublet, $Rh3d_{3/2}$ and $Rh3d_{5/2}$. The curve fitting was also made using Gaussian functions, although it is not very common when it comes to rhodium, due to its asymmetry band. For this case, the more indicated line shape function to be used is the Doniach-Sunjic [16]. Although, some authors have used Gaussian functions for the purpose to do Rh3d curve fitting, for instance [17]. Through the Rh3d curve fitting, it was possible to identify Rh^0 at 312.68 and 307.92 eV, Rh_2O_3 at 313.80 and 309.46 eV and RhO_2 at 315.08 and 310.97 eV. These results are following [17–19]. In PdRh(50:50)/C, it was also possible to identify the Pd3d doublets, $Pd3d_{3/2}$ and $Pd3d_{5/2}$. The curve fitting was also made using Gaussian functions, but the metal oxide observed in PdRh(50:50)/C was different from the metal oxide observed in Pd/C. Pd^0 was observed in 341.18 and 335.92 eV and PdO_2 in 342.62 and 338.06 eV. It is possible to see a small shift in the main peak $Pd3d_{5/2}$, and this can occur by the addition of Rh to the nanomaterial. In PdSn(50:50)/C

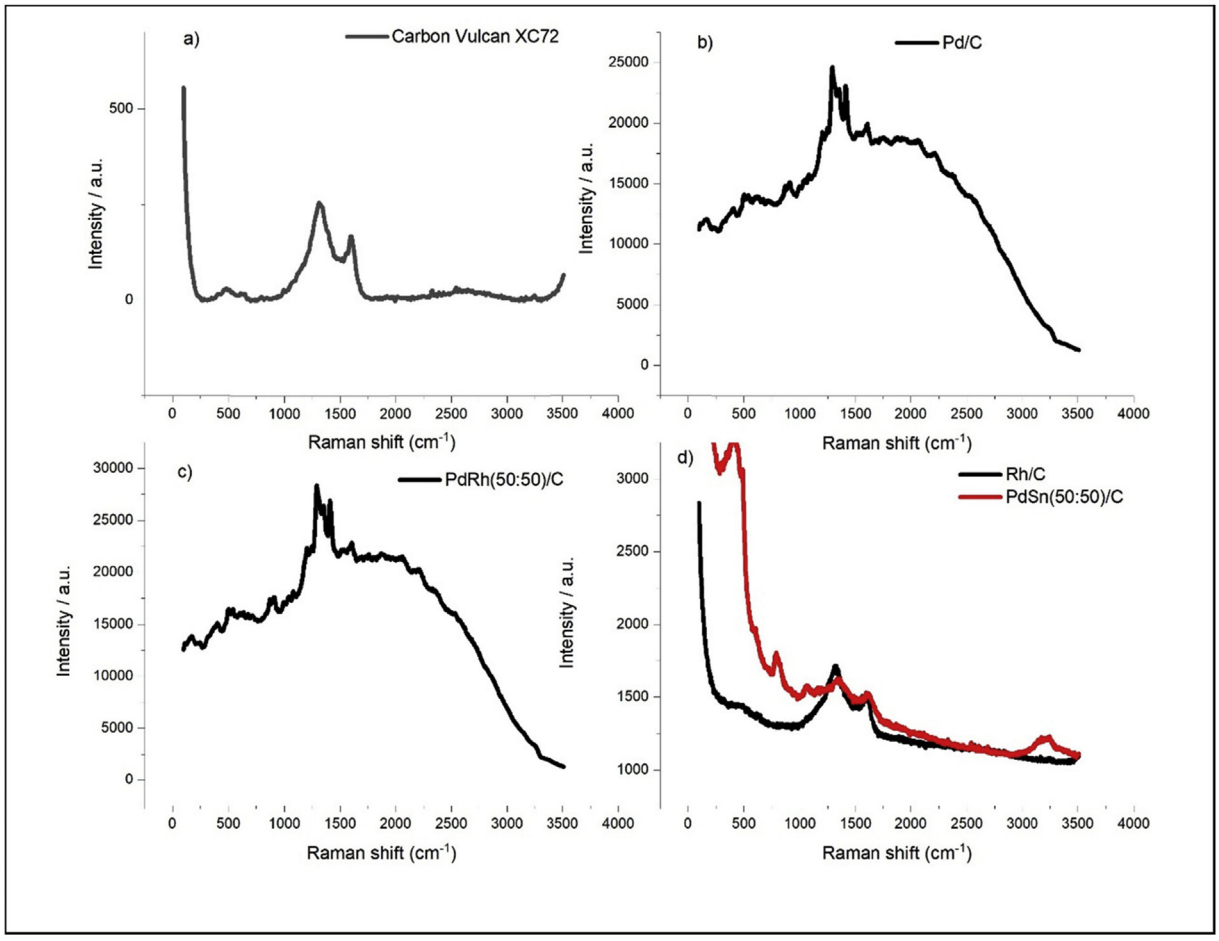

Fig. 1 – Raman spectra of a) Carbon Vulcan XC72, b) Pd/C, c) PdRh(50:50)/C and d) PdSn(50:50)/C and Rh/C.

electrocatalyst, it was also possible to identify the Pd3d doublets, $Pd3d_{3/2}$ at 341.49 eV and $Pd3d_{5/2}$ at 336.21 eV. It is interesting to note that, the Pd3d doublets from PdSn(50:50)/C are very similar to those obtained from PdRh(50:50)/C, this suggests that the addition of a co-catalyst promotes the same effect in Pd3d doublets peaks.

Energy dispersive X-ray spectroscopy and scanning electron microscopy

EDS can provide information about elemental composition in the bulk of the material [20]. The EDS performed in the SEM (Scanning electron microscopy) mode has a depth resolution about 1–3 μm, while XPS has a depth resolution lower than 5 nm [21]. That is why both techniques are complementary, and we expect to see different results between them. Also, this information may help to explain other results obtained by other methods. In supplemental material, S4 and S6 show the spectra obtained by EDS, and as it can be seen, all the metals are present. Pd is observed in Pd/C, Pd and Rh are present in PdRh(50:50)/C, and Pd and Sn are present in PdSn(50:50)/C. Also, in supplemental material, S5 and S7 show the images obtained by SEM. They reveal the topographical and morphological distribution of the material. The white spots may also be attributed to the metal nanoparticles; therefore, we can see proper distribution in the carbon support. These images were taken before any kinds of experiments, but if they were compared after CV, for instance, it would be possible to see the attrition of the material.

Transmission electron microscopy

Figs. 5–10 show the TEM micrographs taken in the bright field mode and the mean Feret's diameter for all materials. Table 1 also shows the Feret's mean diameter for all materials. PdSn(50:50)/C electrocatalyst shows the smallest size while PdRh(50:50)/C electrocatalyst shows the largest one.

X-ray diffraction

Fig. 11 shows the diffraction pattern of Pd/C electrocatalyst and the curve fitting for all crystalline planes. The peak at $2\theta = 24.5°$ is associated with the crystalline plane (002) of the carbon support [22] and it is observed for all materials studied. $2\theta = 40°$, 47°, 68°, 82° and 85° are observed, and it is respectively associated with (111), (200), (220), (311) and (222) crystalline planes (PDF Number 1-1201) characteristic of palladium FCC structure. Fig. 12a and c show the diffraction pattern of PdSn(50:50)/C and PdRh(50:50)/C. In Fig. 12b, it is possible to observe the presence of Pd and Sn atoms through its crystalline structure. The $2\theta = 39°$, 65° and 80° are respectively related to the (111), (220) and (311) crystalline planes of Pd FCC structure (PDF Number 1-1310). $2\theta = 30°$ and 42° are respectively related to the (200) and (211) crystalline planes of Sn tetragonal (PDF Number 1-926). Fig. 12c shows the diffraction

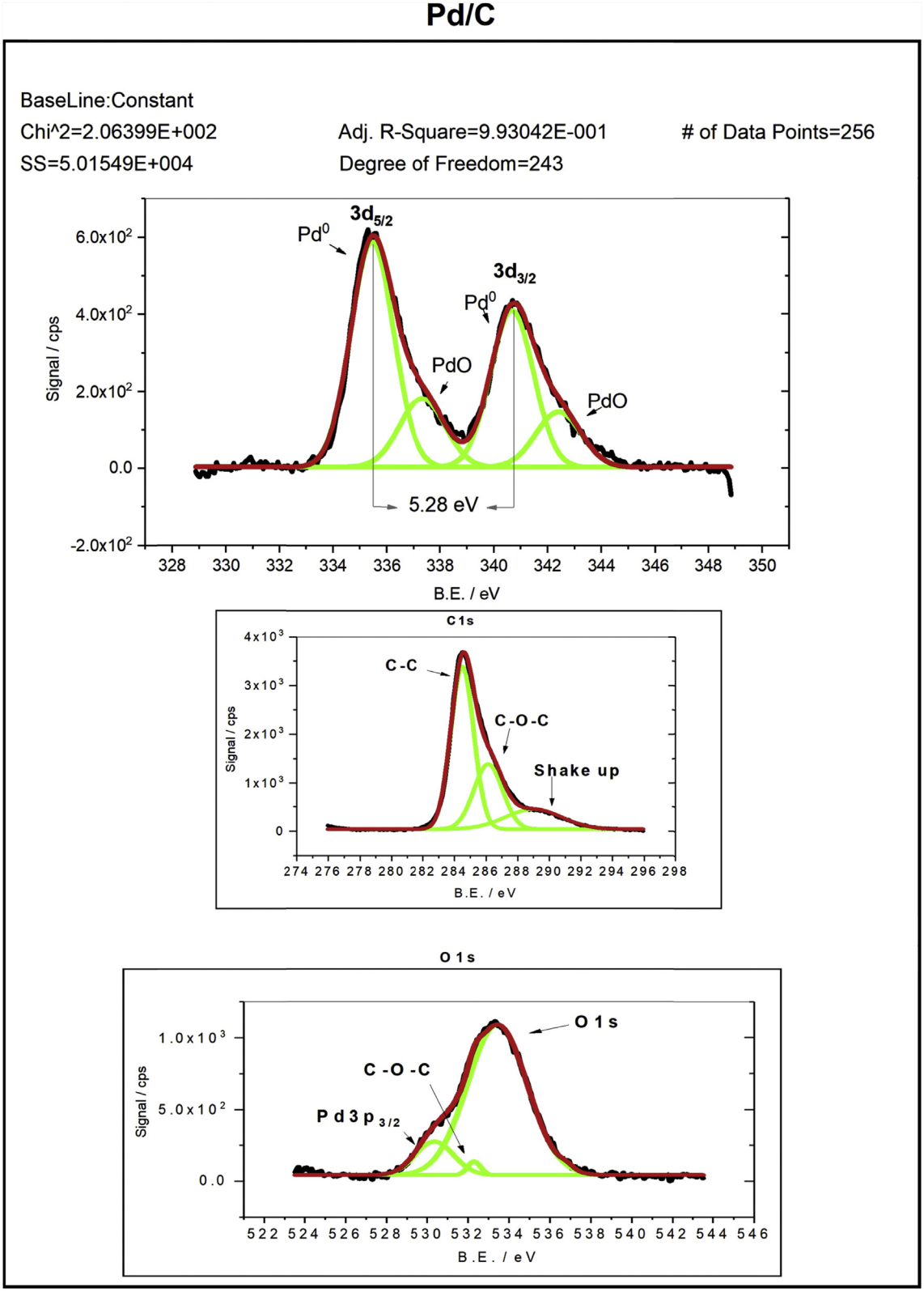

Fig. 2 – XPS spectra of Pd3d band, C1s band and O1s band. The black lines represent the experimental curve, the green lines are the individual curves that were obtained by curve fitting and the red lines are the sum of the green lines. (For interpretation of the references to color in this figure legend, the reader is referred to the Web version of this article.)

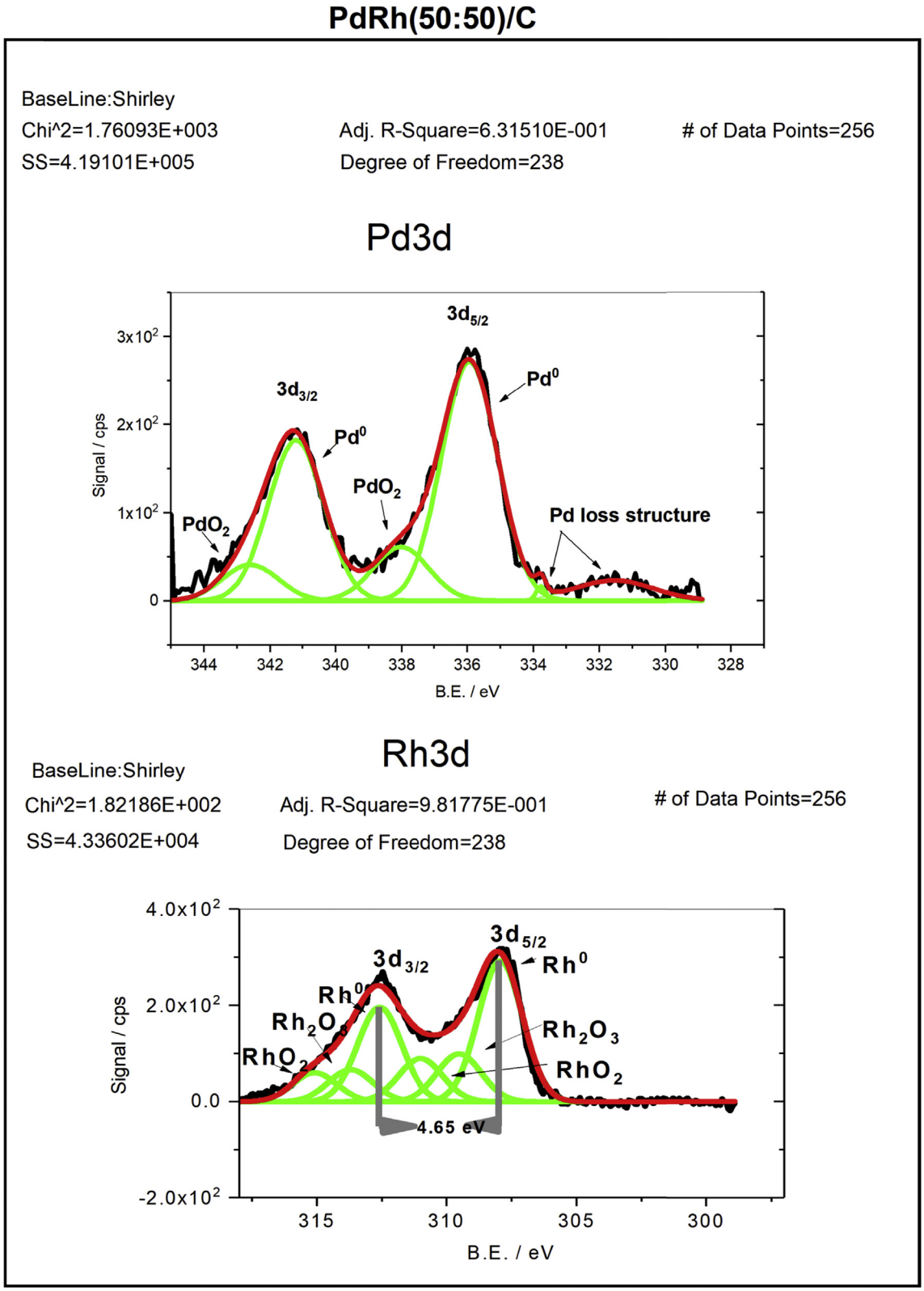

Fig. 3 – XPS spectra of Pd3d band and Rh3d band characteristic of PdRh(50:50)/C. The black lines represent the experimental curve, the green lines are the individual curves that were obtained by curve fitting and the red lines are the sum of the green lines. (For interpretation of the references to color in this figure legend, the reader is referred to the Web version of this article.)

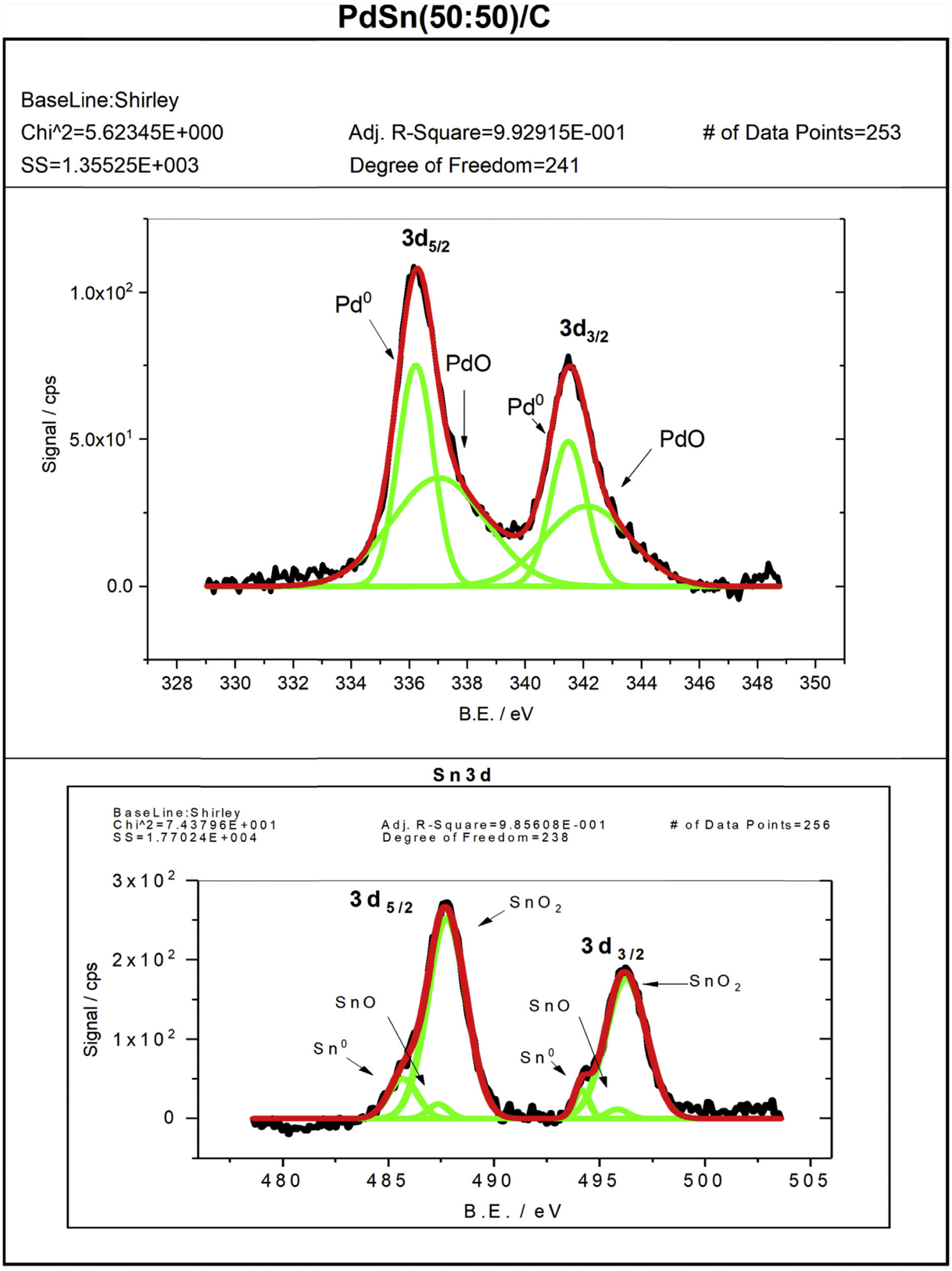

Fig. 4 – XPS spectra of Pd3d band and Sn3d band characteristic of PdSn(50:50)/C. The black lines represent the experimental curve, the green lines are the individual curves that were obtained by curve fitting and the red lines are the sum of the green lines. (For interpretation of the references to color in this figure legend, the reader is referred to the Web version of this article.)

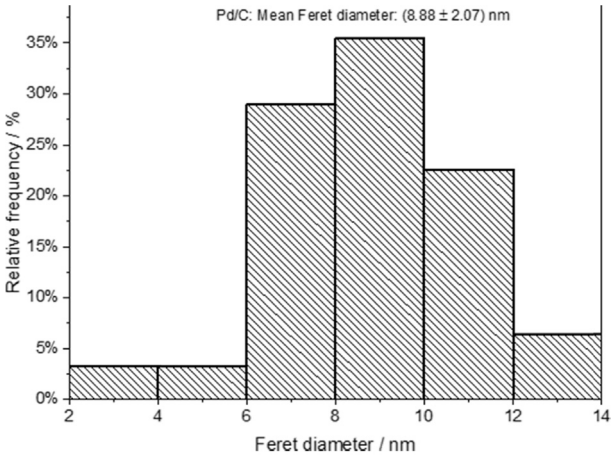

Fig. 5 – Feret diameter distribution of Pd/C electrocatalyst.

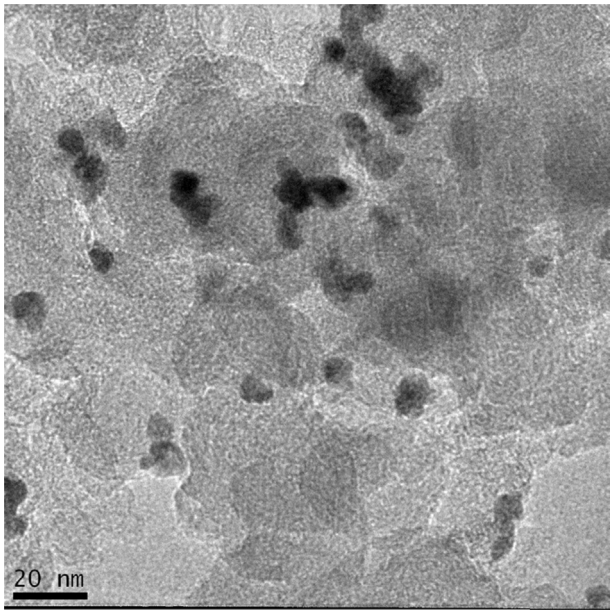

Fig. 6 – TEM image of Pd/C electrocatalyst.

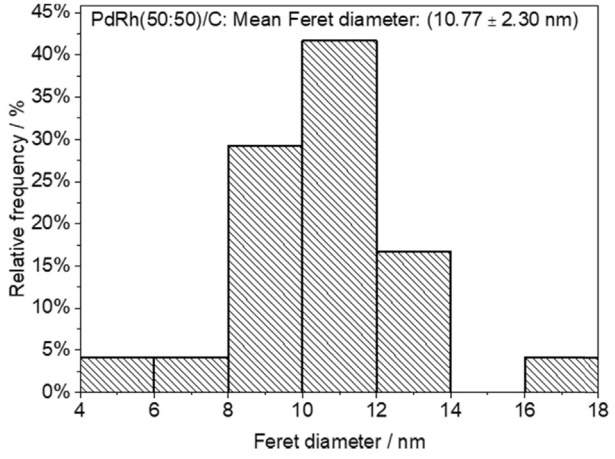

Fig. 7 – Feret diameter distribution of PdRh(50:50)/C electrocatalyst.

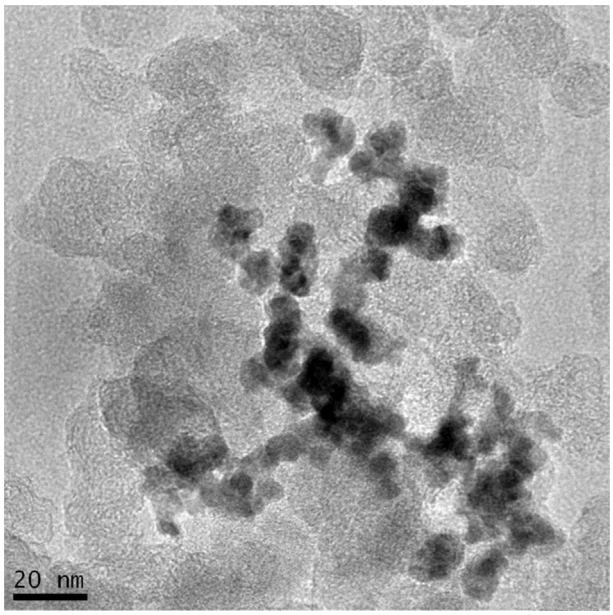

Fig. 8 – TEM image of PdRh(50:50)/C electrocatalyst.

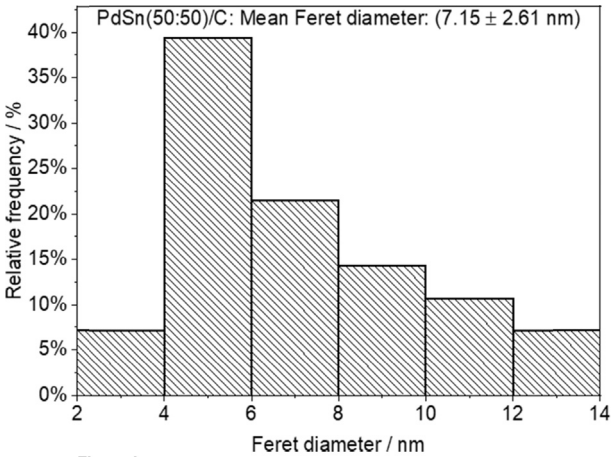

Fig. 9 – Feret diameter distribution of PdSn(50:50)/C electrocatalyst.

pattern of PdRh(50:50)/C electrocatalyst and Fig. 12d shows the curve fitting for all crystalline planes. $2\theta = 40°$, 47°, 69° and 84° are observed, and it is respectively associated with (111), (200), (220), (311) crystalline planes characteristic of rhodium FCC structure [3], while the other peaks are related to the palladium FCC structure.

Cyclic voltammetry, linear sweep voltammetry and chronoamperometry

Fig. 13 shows the cyclic voltammetry of Pd/C, PdSn(50:50)/C and PdRh(50:50)/C electrocatalysts in 1.0 mol L^{-1} KOH + 1.0 mol L^{-1} EtOH. Fig. 14 shows the linear sweep voltammetry of Pd/C, PdSn(50:50)/C and PdRh(50:50)/C electrocatalysts in 1.0 mol L^{-1} KOH + 1.0 mol L^{-1} EtOH. All the curves represent the linear anodic sweep and the electrocatalytic activity toward ethanol oxidation. As it can be seen, Pd/C and PdSn(50:50)/C exhibit the lowest onset potential, while

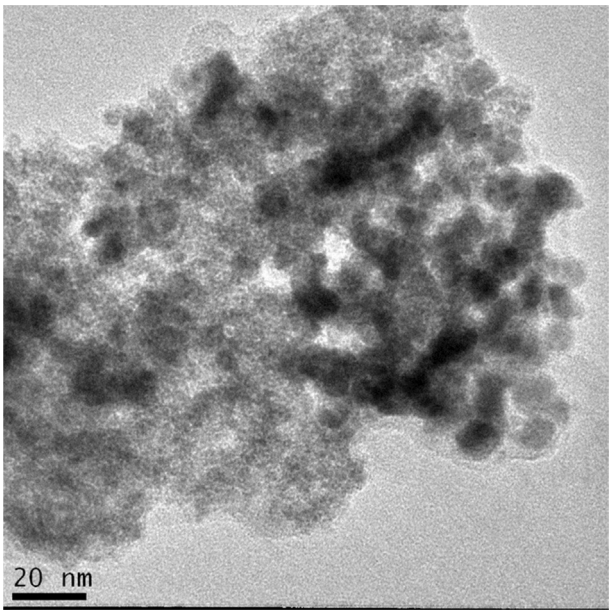

Fig. 10 – TEM image of PdSn(50:50)/C electrocatalyst.

PdRh(50:50)/C exhibits a higher one. Besides that, PdSn(50:50)/C shows the highest final current density when compared to the other materials. Fig. 15 shows the chronoamperometric curve for Pd/C, PdSn(50:50)/C and PdRh(50:50)/C in 1.0 mol L^{-1} KOH +1.0 mol L^{-1} EtOH at −0.35 V. PdSn(50:50)/C and Pd/C show a similar final density current value, but PdSn(50:50)/C is slightly higher. It should be emphasized that because of the coating technique employed, ultrathin porous coating, the current density values are smaller than electrode prepared by thin porous coating.

Table 1 – Feret's mean diameter.

	Pd/C	PdRh(50:50)/C	PdSn(50:50)/C
Feret's mean diameter	(8.88 ± 2.07 nm)	(10.77 ± 2.30 nm)	(7.15 ± 2.61 nm)

Atennuated total reflection - Fourier transform infrared

Figs. 16–18 and in supplemental material S8, S9 and S10 show the FTIR spectra, product formation and the 1st derivative of the product formation for all the materials studied. They were performed at in situ conditions. For all of them, it was possible to see the asymmetric stretching of carbon dioxide (2343 cm^{-1}), the stretching of the CO bond of carbonate ion (1376 cm^{-1}), the symmetric stretching of acetate (1407 cm^{-1}) and the rocking of acetaldehyde (928 cm^{-1}) [3,23]. All the bands were deconvolved using Lorentzian and Gaussian functions [3,23].

Fuel cell experiment

As we can observe in Figs. 19 and 20, PdSn(50:50)/C promotes the best DEFC performance, 20 mW cm^{-2} against 15 mW cm^{-2} of Pd/C. Similarly, to the other results in the literature [24,44] Pd/C and PdSn(50:50)/C have a similar performance in DEFC, but PdSn(50:50)/C is slightly better when compared to Pd/C.

Discussion

We can notice that in Fig. 1d Rh/C and in Fig. 1a Carbon Vulcan XC72, the peaks are very similar. This occurs, probably, because the metals are not bonded to the carbon atoms. They do not modify the carbon structure. Therefore, it is possible that rhodium atoms are bonded only with oxygen or hydrogen atoms. But in Fig. 1b–d PdSn(50:50)/C, it can be seen a modification in the D′, G, D3, D and D4 bands of the Carbon Vulcan XC72. A lot of new peaks emerge and overlap with D′, G, D3, D, and D4 bands. This change can be explained by the fact that palladium atoms were incorporated on the carbon structure. Nanoparticles of palladium anchored to the carbon nanostructure tend to form π stable complexes with the unsaturated C-C bond C_{π}. The unsaturated C-C bond can act like a donator of efficient active sites to form bondings with

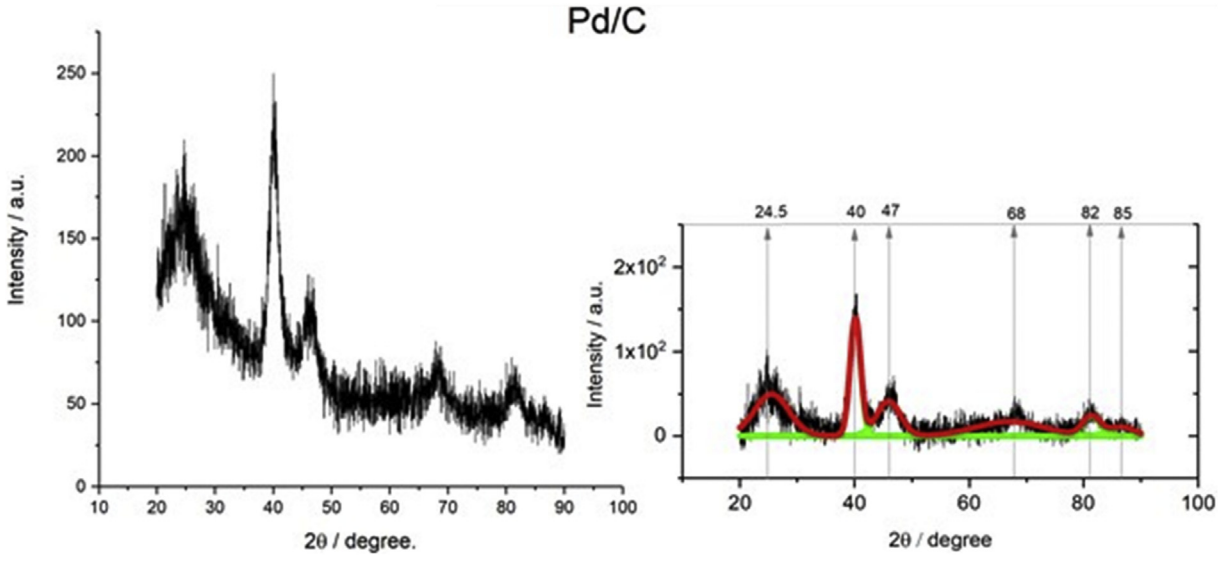

Fig. 11 – X-ray diffraction pattern for Pd/C and curve fitting for all crystalline planes.

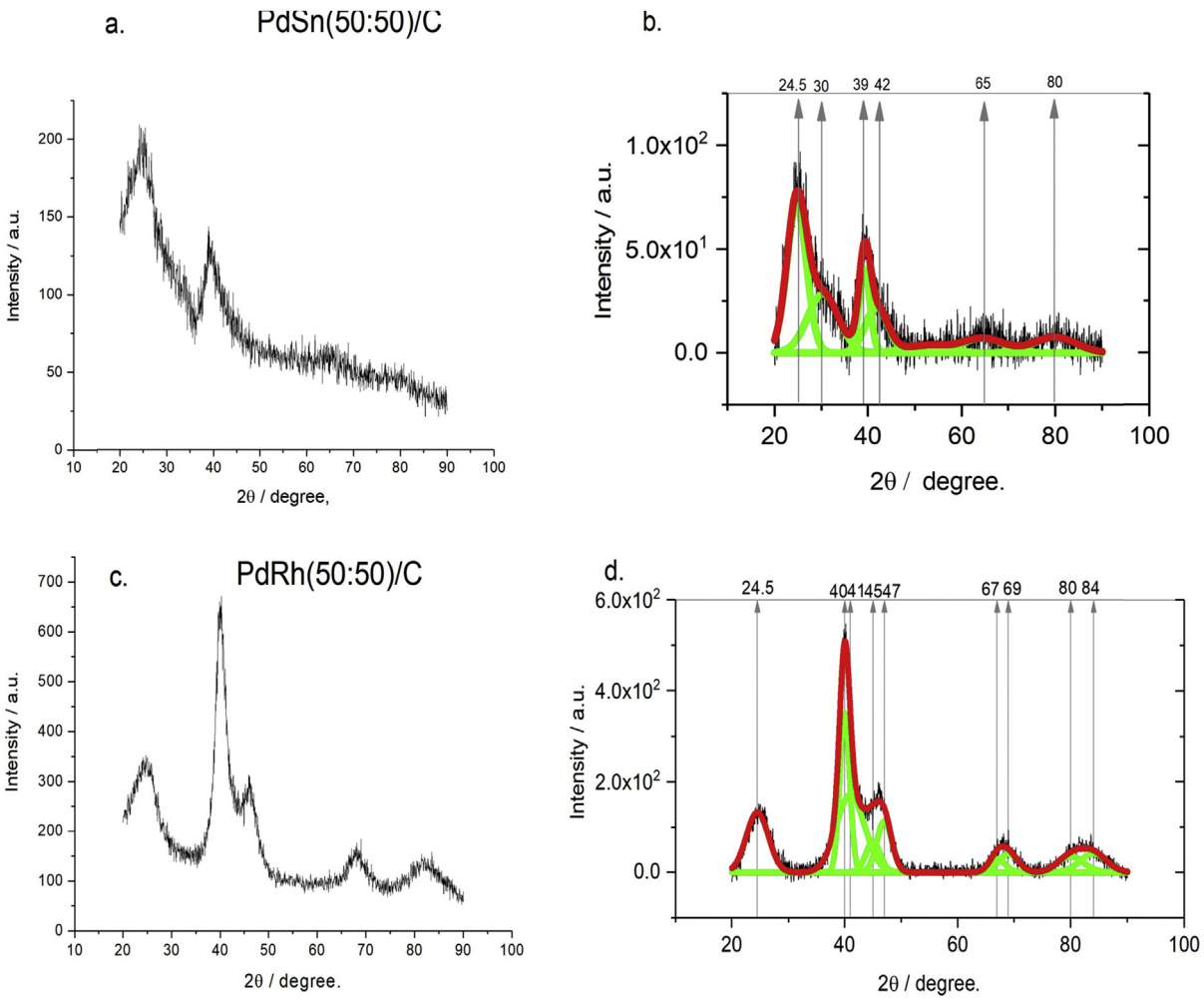

Fig. 12 – X-ray diffraction pattern for PdSn(50:50)/C and PdRh(50:50)/C and curve fitting for all crystalline planes.

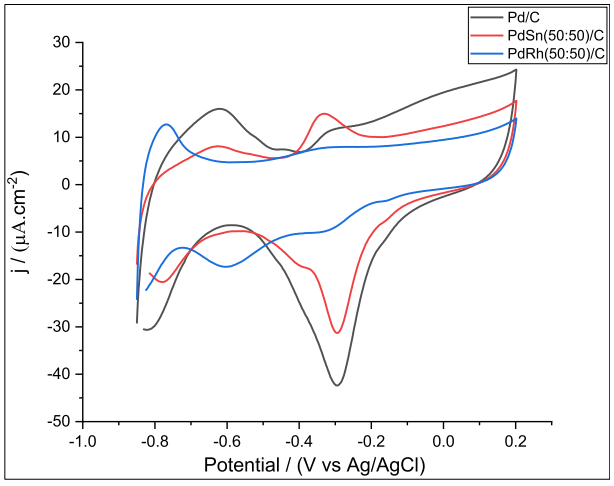

Fig. 13 – Cyclic voltammetry for Pd/C, PdSn(50:50)/C and PdRh(50:50)/C. The electrolyte solution is 1.0 mol L^{-1} KOH + 1.0 mol $L^{-}1$ EtOH. The swept potentials were −0.85 V up to 0.2 V. The Electrochemical Surface Area (ECSA) used here is 12.26 cm^2 for Pd/C; 7.54 cm^2 for PdSn(50:50)/C and 5.32 cm^2 for PdRh(50:50)/C. To measure the ECSA we have followed [43].

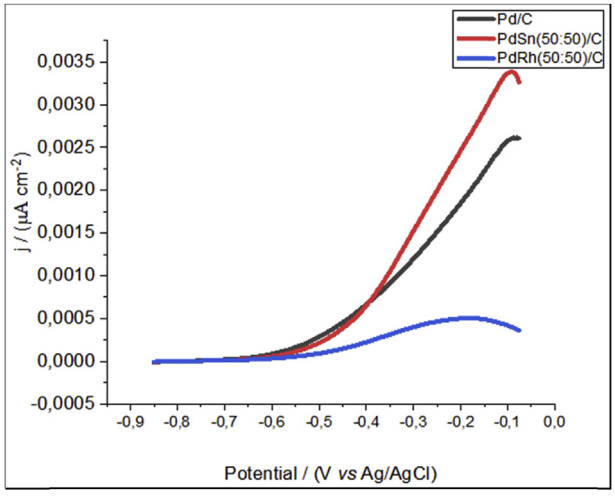

Fig. 14 – Linear sweep voltammetry for Pd/C, PdSn(50:50)/C and PdRh(50:50)/C. The electrolyte solution is 1.0 mol L^{-1} KOH + 1.0 mol $L^{-}1$ EtOH. The swept potentials were −0.85 V up to −0.05 V.

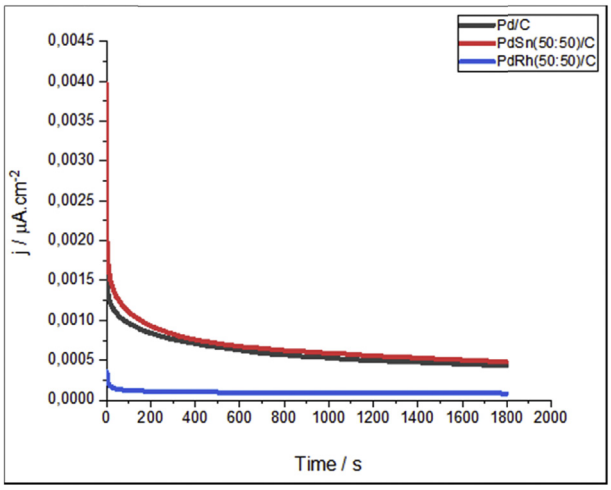

Fig. 15 – Chronoamperometry curve for Pd/C, PdSn(50:50)/C and PdRh(50:50)/C. The electrolyte solution is 1.0 mol L^{-1} KOH + 1.0 mol L^{-1} EtOH. The applied potential was −0.35 V.

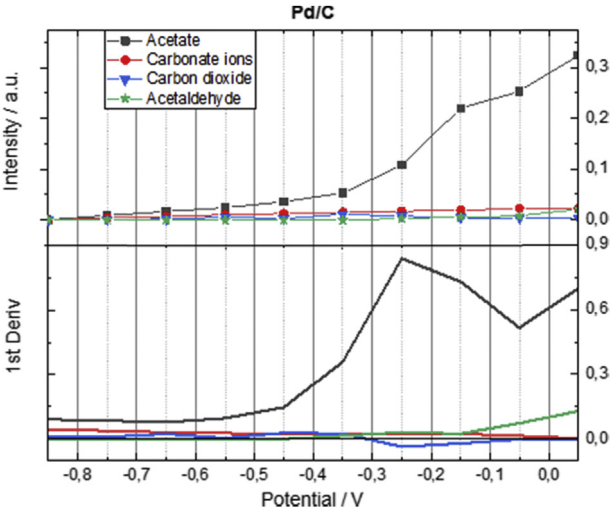

Fig. 16 – Product formation vs potential applied and the 1st derivative of the products formation vs potential applied for Pd/C.

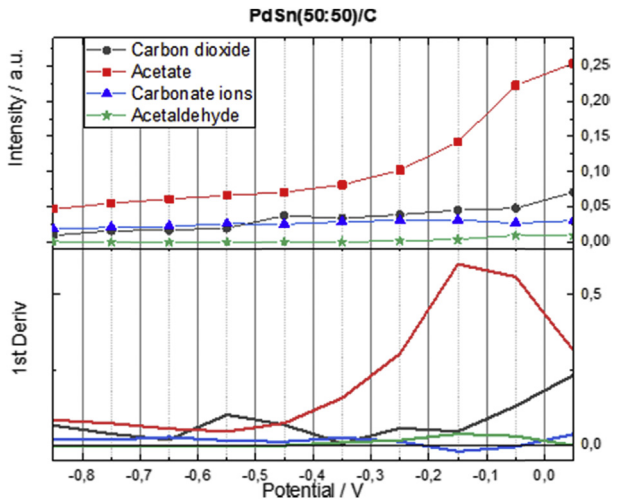

Fig. 17 – Product formation vs potential applied and the 1st derivative of the products formation vs potential applied for PdSn(50:50)/C.

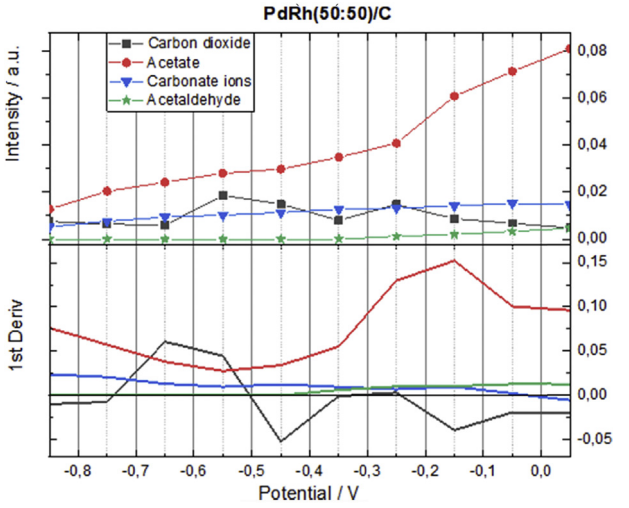

Fig. 18 – Product formation vs potential applied and the 1st derivative of the products formation vs potential applied for PdRh(50:50)/C.

palladium atoms, and they also act in the formation of hybrids Pd-C bonds [25]. It was not possible with Raman spectroscopy to observe some metal oxides, like, for instance, 284 cm^{-1} (RhO_3), 650 cm^{-1} (PdO) and 523 cm^{-1} ($PdRhO_2$) [26]. The signal to noise ratio was feeble and, besides that, the measure was not made on the surface, instead, it was made in bulk. But it was also possible to observe metal oxides in the surface using x-ray photoelectron spectroscopy technique. Even though metal oxides were not formed at the bulk, many different peaks emerged as the presence of palladium atoms increased. This result is supported by Ref. [27]. This can be explained because the disorder promoted in the crystalline structure of Carbon Vulcan XC72, due to the presence of palladium atoms, it decreases the ratio ($I_D/I_G = 2 \rightarrow 1.95$), where I_D and I_G are the D and G band intensity and relaxes the selection rules which concerns to the crystal momentum conservation. That is why the phonons through the Brillouin zone contribute to a large Raman scattering according to the intensity of the symmetry break caused by the perturbation introduced by palladium atoms on the carbon structure.

Concerning XPS results, the formation of PdO_2 in PdRh(50:50)/C can be attributed to the sodium borohydride reduction method employed [28]. The release of H_2 and H+ in aqueous medium changes the surface of the palladium atoms, leading to a significant amount of PdO_2 that is stable in this medium. Besides that, some authors have reported the presence of PdO_2 through XPS measurements [29,30]. The distance between the experimental Rh3d doublets peaks center is about 4.65 eV, while (Moulder, 1992) [13] report this distance as 4.75 eV, also showing a good agreement between the results and the literature. The curve fitting in PdSn(50:50)/C was also

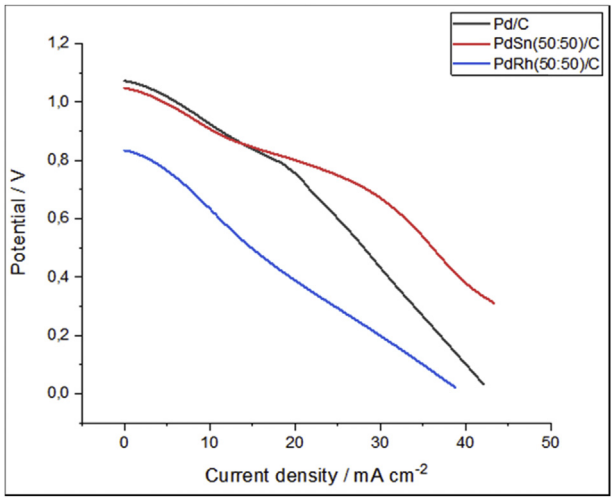

Fig. 19 – Polarization curve of a 5 cm^2 DEFC at 50°C using 1.0 mol L^{-1} KOH and 2.0 mol L^{-1} of EtOH for all electrocatalysts.

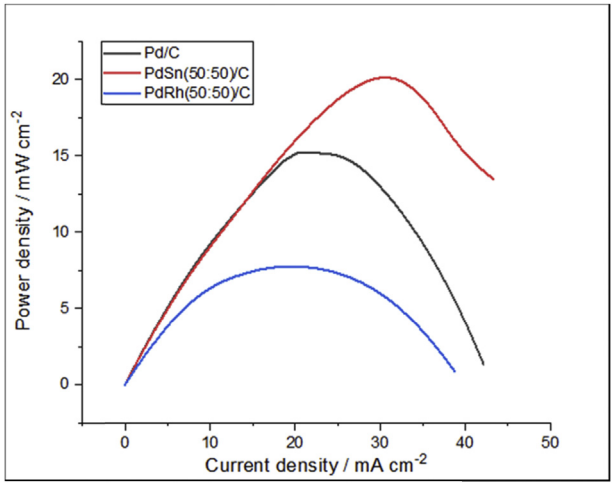

Fig. 20 – Power density curve of a 5 cm^2 DEFC at 50°C using 1.0 mol L^{-1} of KOH and 2.0 mol L^{-1} of EtOH for all electrocatalysts.

made using Gaussian functions, but the metal oxide observed was PdO. PdO formation can also be attributed to the synthesis method employed [28], but the influence of the synthesis in the formation of PdO in PdRh(50:50)/C and PdO_2 in PdSn(50:50)/C remains a challenge. But it is very known that the most likely of palladium species is the PdO [28]. Curve fitting showed the presence of PdO approximately at 337.03 eV and 342.20 eV Sn3d doublets peaks were also identified in PdSn(50:50)/C. Sn^0 doublet was observed in 485.67 eV and 494.17 eV. The experimental distance between the two peaks is 8.5 eV, the same value reported in Ref. [13]. But it is very interesting to note the small shift to a higher value of binding energy, 485.67 eV, while [13] reports as 484.65 eV. This difference can be explained by the fact that Pd and Sn may have formed a metallic alloy like it was mentioned before. $[SnO]3d_{5/2}$ was observed in 487.38 eV and $[SnO]3d_{3/2}$ was observed in 495.88 eV.

It was also possible to observe SnO_2 species. $[SnO_2]3d_{5/2}$ was observed at 487.74 eV and $[SnO_2]3d_{3/2}$ was observed at 496.25 eV. These results are following [13,31,32]. Both tin and rhodium oxide species are present in these materials mainly due to the method of synthesis employed. Also, the ambient exposure can influence the formation of these species. But the dynamics of how these metal oxides are formed need to be explored better using complementary physical and chemical characterization techniques. The chemical shifts caused by the presence of metal oxides can be explained by the effective charge potential change on palladium or rhodium or tin and oxygen atoms [14]. When Palladium or rhodium or tin is bonded to oxygen, which has a higher electronegativity, a charge transferred to oxygen makes palladium or rhodium or tin become more positively charged, so the binding energy increases. That's why we can observe small shifts to higher values of binding energy for PdO or PdO_2 when compared to Pd^0. Also, for Sn^O or SnO_2 when compared to Sn0, and also for RhO_2 and Rh_2O_3 when compared to Rh^0. Due to large amounts of carbon in the sample, the intensity of C1s band is higher when compared to the intensity of Pd3d, O1s, Rh3d, and Sn3d. All these materials, Pd/C, PdRh(50:50)/C and PdSn(50:50)/C, exhibited the same C1s features. Making curve fitting on C1s, it was possible to observe different types of bonds. There were observed bonds of the type (C-O-C), with binding energy approximately as 286.13 eV for Pd/C; 285.80 eV for PdRh(50:50)/C; 285.88 eV for PdSn(50:50)/C there were also observed bonds of the type (C-C) assign to the sp^2 carbon, with binding energy approximately as 284.57 eV for Pd/C; 284.83 eV for PdRh(50:50)/C; 285.18 eV for PdSn(50:50)/C and the satellite-peak of shake-up type of $\pi \rightarrow \pi^*$ transition at approximately 289.13 eV for Pd/C; 289.43 eV for PdRh(50:50)/C; 288.67 eV for PdSn(50:50)/C. All these carbon bonds results agree with [33–35]. Due to the ambient exposure of these materials and the reduction method used [28], it was possible to observe for all of them, the O1s valence spectra band. Unfortunately, it was not possible to observe the metal oxide bond through the O1s band, probably, because the main peak at 533.38 eV for Pd/C; 533.51 eV for PdRh(50:50)/C; 533.50 eV for PdSn(50:50)/C is too intense. But, through curve fitting, also using Gaussian functions, it was possible to observe the C-O-C bond at 532.34 eV for Pd/C; 532.15 eV for PdRh(50:50)/C; 530.98 eV for PdSn(50:50)/C and the $Pd3p_{3/2}$ at 530.48 eV for Pd/C; 530.61 eV for PdRh(50:50)/C; 530.08 eV for PdSn(50:50)/C. These results are following [13.33]. The atomic composition of metal oxides and metals were obtained by XPS and EDS analyses. In theory, both techniques have their peculiarities. For instance, XPS analysis can be made at the interface between the material, and the environment and this region comprehends about 5 nm at the surface of the material [17]. While EDS can investigate the bulk of the material, reaching a few micrometers instead of nanometers [14,20]. So, we can say that both techniques are complementary. It is expected to observe some differences between these techniques because the samples prepared have a few micrometers of thickness. The quantitative analysis was made using the relation [13,36]:

$$I = n f \sigma \theta y \lambda A T \quad (1)$$

where **I** is the intensity of a specific spectral peak, **n** is the

number of atoms of the element per cm^3 of sample, **f** is the x-ray flux in photons/$cm^2 sec$, σ is the photoelectric cross section for the atomic orbital of interest in cm^2, θ is an angular efficiency factor for the instrumental arrangement based on the angle between the photon path and detected electron, **y** is the efficiency in the photoelectric process for formation of photoelectrons of the normal photoelectron energy, λ is the inelastic mean free path, **A** is the area of the sample from which photoelectrons are detected and **T** is the detection efficiency for electrons emitted from the sample.

$$n = I/(f\sigma\theta\nu\lambda AT) \quad (2)$$

defining a new quantity, called **S** (atomic sensitivity factor), and considering the strong line between two elements, then:

$$\frac{n_1}{n_2} = \{(I\}_1/S_1)/(I_2/S_2) \quad (3)$$

the photoelectric cross section used was the theoretical one proposed by Scofield [37]. Generalizing the expression above, we have:

$$C_x = \frac{n_x}{\sum_i n_i} = (I_x/S_x) \Big/ \left(\sum_i I_i/S_i\right) \quad (4)$$

where C_x is the atomic fraction of any constituent in a sample.

Table 2 shows the results of all the materials studied. It is clear the difference obtained by the two techniques. XPS measurements revealed the presence of metal oxides and metals, while EDS measurements revealed only the presence of metals. But, EDS measurements were closer to the nominal compositions than XPS measurements. This can be attributed to the randomness of the metal oxide formation during the metal salts reduction process. Electrocatalysis is a surface phenomenon, so the XPS results can provide wealth information that may explain many results obtained by other techniques, like, for instance, cyclic voltammetry and Fuel Cells experiment. It is noteworthy that PdSn(50:50)/C has a significant amount of SnO_2 species and a considerable amount of PdO. That is why we had good results obtained by CV and polarization curves also proving that the bifunctional mechanism is prominent in this material. It can also be noted that palladium atoms in PdSn(50:50)/C do not present intense bound with carbon at the bulk of the material. This can be observed through the less intense new peaks in Raman spectroscopy at Fig. 1. Also, this can provide more active sites for palladium atoms to oxidize the fuel. In fact, Table 2 shows that the EDS results for PdSn(50:50)/C have a lower content of palladium atoms at the bulk when compared to the other materials. It is obvious that both techniques are complementary, while EDS can provide information about the bulk of the material, XPS can provide information on the surface of the material. Besides that, palladium atoms tend to be bond with carbon structures, as it can be observed by the Raman spectroscopy results, and XPS revealed that the second metal (Rh or Sn) tends to be observed at the surface of the material, in form of oxide as in the case of tin atoms, and in metallic form as in the case of rhodium atoms.

Table 2 – Atomic composition of metal oxides and metals. A comparison between XPS, EDS and nominal composition.

	XPS	EDS	Nominal composition
Pd/C			
Pd^0	75%	100%	100%
PdO	25%		
PdO_2			
PdRh(50:50)/C			
Pd^0	32%	60%	50%
PdO			
PdO_2	6%		
Rh^0	38%	40%	50%
RhO_2	11%		
Rh_2O_3	13%		
PdSn(50:50)/C			
Pd^0	17%	55%	50%
PdO	21%		
PdO_2			
Sn^0	6%	45%	50%
SnO	2%		
SnO_2	54%		

Figs. 5–10 show the TEM images and the Feret's size distribution. Pd/C shows a good dispersion over the support, but some nanoparticles are still too close to each other, leading to a higher nanoparticle's mean Feret's diameter when compared to PdSn(50:50)/C. Also because of this agglomeration, PdRh(50:50)/C has shown a higher Feret's mean diameter. It is also interesting to notice the possible Z contrast between the metal nanoparticles and the carbon support or the different crystal orientations, which at the end turn into possible differentiate of the metals nanoparticles. The agglomerations observed for all materials are consistent with some results in the literature [17,38]. The excess of agglomeration can lead to a little availability of nanoparticle's active sites, decreasing the electrocatalytic activity, that is why we can also attribute the good electrocatalytic activity of PdSn(50:50)/C. Despite this, all the materials showed a narrow mean Feret's diameter distribution, characteristic of sodium borohydride reducing agent [17].

All curves obtained by curve fitting in the XRD experiments are shown in green, and they correspond to the most intense crystalline planes. All other crystalline planes are much less intense, and besides that, tin exhibits a lot of narrow and strait peaks, making it difficult to do curve fitting. Nevertheless, it is still possible to observe the presence of tin and palladium atoms by XRD. It is also important to note that the measure is done at the bulk, so it wasn't possible to observe the presence of metal oxides as we can observe in XPS. Because of the interference caused by the tin crystalline structure, it was also not able to identify the presence of possible metallic alloy. Because SNR was not high enough, the identification of the lattice parameter modifications in palladium and rhodium materials were compromised.

The lower onset potential observed in Pd/C and PdSn(50:50)/C is attributed to the capability of production of intermediate products of ethanol oxidation. The ATR-FTIR results will show this forward. Besides that, the best performance for EOR observed through PdSn(50:50)/C can be ascribed by the high rate of metal oxide species (XPS), to the high availability of active sites for ethanol to be adsorbed (Raman spectroscopy) and to the lowest Feret's mean diameter (TEM). So, we can again infer that the bifunctional mechanism is genuinely prominent and essential for this material [11,39]. Fig. 15 shows the chronoamperometric curve for Pd/C, PdSn(50:50)/C and PdRh(50:50)/

C in 1.0 mol L^{-1} KOH + 1.0 mol L^{-1} EtOH and at −0.35 V. It is interesting to notice that it is not possible to observe the potentiostatic transient in all these materials. But it is possible to simulate the stability and evaluate the electrocatalytic activity of these materials toward ethanol oxidation. PdSn(50:50)/C and Pd/C show a similar final density current value, but PdSn(50:50)/C is slightly higher. Again, the surface composition of PdSn(50:50)/C can play a decisive role in the performance of ethanol oxidation. As we can see further through FTIR results, PdRh(50:50)/C has shown a poor behavior compared to the other materials, because of the poisoning effect caused by the intermediate product of ethanol oxidation [3].

The electrochemical activity toward ethanol oxidation can be explained through FTIR results, and it is possible to propose a reaction mechanism qualitatively. The use of Pd/C as anode electrocatalyst promotes the formation of acetate rather than other ethanol oxidation products. It is also interesting to notice that the variation in products formation along the applied potentials is remarkably lower compared to the other materials studied. The current density observed in Figs. 14 and 15 is mainly attributed to the acetate formation. PdSn(50:50)/C shows to be a promising material because the CO_2 production is relatively higher, the acetate production is also higher, and the carbonate ions production is lower for almost all potentials applied. PdRh(50:50)/C also has significant production in CO_2 and acetate, but the carbonate ions production is even higher, and because of this higher production the electrocatalytic activity decrease, due to the carbonate ions can block the active sites of the electrocatalysts [3,38,40]. It is important to stress out that the kinetics of the overall reaction is fast for all materials studied [23]. The carbonate ions production is smaller for PdSn(50:50)/C, and the acetate/CO_2 ratio in −0.35 V is also smaller, suggesting that despite the mechanism ran in a parallel mode (incomplete leading to acetate, carbonate ions and acetaldehyde and complete leading to CO_2), PdSn(50:50)/C has a predominant complete mechanism over all other materials studied, as we can see in the Fig. 17. That is why we can also observe a better current density in chronoamperometric experiments for PdSn(50:50)/C. Now we can understand why PdSn(50:50)/C has a better performance in electrochemical and in fuel cell experiments. This material has 54% of SnO_2 on the surface, contributing to the CO_2 formation through the bifunctional mechanism and this is supported in the literature by Ref. [41]. Besides that, a lower amount of Pd atoms were bonded to the carbon structure, leading to a larger area of Pd active sites, as we can observe through the Raman spectroscopy results. PdRh(50:50)/C has produced a significant amount of carbonate ions, and this can block the active sites of Pd and Rh, diminishing the performance in DEFC. Besides that, PdRh(50:50)/C showed a significant variation in CO_2 production, in such a way that acetate/CO_2 ratio was higher when compared to the other materials. Also, PdSn(50:50)/C presented a better performance in the diffusional regime when compared to Pd/C, and the tin effect can explain this along with the synthesis employed.

Methods

Pd/C, PdSn(50:50)/C and PdRh(50:50)/C electrocatalysts (20 wt % of metals loading) were prepared using $RhCl_3.xH_2O$, $Pd(NO_3)_2.2H_2O$, Tin(II) Chloride dihydrate ($SnCl_2.2H_2O$) as metals sources, all from Sigma Aldrich and the support used was Carbon Vulcan XC72 (Cabot). The reducing agent used was sodium borohydride (Sigma Aldrich) dispersed in a solution of 0.01 mol L^{-1} NaOH (a stabilizing agent). The metal salts were added in a mixture of water/2-propanol (50/50, v/v) along with Carbon Vulcan XC72. The mixture was taken to an ultrasonic homogenizer for 10 min and then the reducing agent was added swiftly under stirring at room temperature acting for 1 h. Immediately after this, the mixture was filtered and washed with (milli-Q water) and then dried at 70 °C for 2 h [3]. The electrocatalysts were characterized by Transmission Electron Microscopy (TEM) analysis. The equipment used was the JEOL JEM-2100 electron microscope operated at 200 kV. This technique was used to determine the size distribution, morphology, and nanoparticles Feret's mean diameter. X-ray diffraction (XRD) analysis was performed on Rigaku Diffractometer model Miniflex II using CuKα radiation source (λ = 0.15406 nm). The diffractograms were recorded from $2\theta = 20°$ to 90° with a step size of 0.05° and a scan time of 2 s per step. The cyclic voltammetry (CV) and chronoamperometry measurements were carried out in the Potentiostat PGSTAT30 AutoLab. The working electrode was prepared by the ultrathin porous coating technique, which consists in an electrode of 3 mm of diameter, 8 mg of catalyst, 20 μL of Nafion 5%, 600 μL of milli-Q H_2O and 400 μL of isopropyl alcohol. The reference electrode was Ag/AgCl (3.0 mol L^{-1} KCl) and the counter electrode was a Pt plate with 2 × 2 cm of dimensions. The electrochemical measurements were realized in the presence of 1.0 mol L^{-1} of ethanol + 1.0 mol L^{-1} KOH solutions saturated with N_2. Direct ethanol fuel cell (DEFC) experiment was done using a single cell with 5 cm^2 of area. The temperature was set to 60 °C for the fuel cell and 85 °C for the oxygen humidifier. All electrodes were made by 1.0 mg of metal per cm^2 in the anode and the cathode. In all experiments, a commercial Pt/C (BASF) was used as the cathode. All the electrocatalysts were painted over a carbon cloth in the form of a homogeneous dispersion prepared using Nafion solution (5 wt%, Aldrich). After the preparation, the electrodes were hot pressed on both sides of a Nafion ^{R} 117 membranes at 125 °C for 3 min under a pressure of 247 kgf cm^{-2}. Before being used, the membranes were exposed to 6 mol L^{-1} KOH for 24 h at least. The fuel, 2.0 mol L^{-1} of ethanol and 1.0 mol L^{-1} KOH were delivered at 1.0 mL min^{-1} and the oxygen flow was regulated at 150 mL min^{-1}. Polarization curves were obtained using a Potentiostat/galvanostat PGSTAT302N AutoLab. The spectroelectrochemical IN-SITU measurements were made using the Nicolet 6700 FT-IR spectrometer equipped with an MCT detector cooled with liquid nitrogen, the electrochemical cell made with Nafion and ATR accessory Miracle Pike (which the internal reflection element is ZnSe). The working electrodes and the operational parameters concerning the electrochemical view are the same as the electrochemical measurements. The FTIR parameters can be found in reference [3] and the background collection is performed at −0.85 V. Raman spectroscopy was performed using the MacroRam Raman spectroscopy by Horiba Scientific. The wavelength used was 785 nm and all the materials were measured using 7% of laser power, 40 s set for the acquisition and real-time

display and the accumulation was equal to 5. X-ray photoelectron spectroscopy was done using an aluminum source and strainer energy equal to 44 eV. The pressure during the analysis was approximately 5.6 10^{-8} mbar and the x-ray spot was about 10 mm in diameter. The samples were pressed at 247 kgf cm^{-2} for 5 s and after this, it was placed on a carbon ribbon. For the determination of the metallic elements present in the electrocatalysts, (SEM) Scanning Electron Microscope was used. The microscope is the Philips XL 30, whose electron beam is of the order of 20 KeV coupled to an EDAX DX-4 microanalyzer. The powder samples were placed in a copper sample port using a double-sided tape [42].

Conclusion

Pd/C, PdSn(50:50)/C and PdRh(50:50)/C electrocatalysts showed some modifications in the D and G bands of the carbon, and this fact is related to the electrochemical oxidation of the ethanol. We also show the difference in quantification using two different techniques, XPS and EDS, in which the first one can identify different chemical states of the metals in question. Besides that, XPS revealed 54% of SnO_2 in the surface of PdSn(50:50)/C electrocatalyst, and this can endorse the bifunctional mechanism observed in FTIR spectra and electrochemical measurements. PdSn(50:50)/C proved to be the best material to be used in a DEFC when compared to Pd/C and PdRh(50:50)/C electrocatalysts, because the acetate/CO_2 ratio is lower than the other ones.

Author contributions statement

E.H.F and A.O analyzed the results, C.E.D.R, J.N and R.M.P conduced the experiments and R.L did the XPS measurements.

Additional information

The authors declare that this work does not have any financial interest nor non-financial competing interests.

Appendix A. Supplementary data

Supplementary data to this article can be found online at https://doi.org/10.1016/j.ijhydene.2018.11.049.

REFERENCES

[1] Akhairi MAF, Kamarudin SK. Catalysts in direct ethanol fuel cell (DEFC): an overview. Int J Hydrogen Energy 2016;41:4214–28. https://doi.org/10.1016/j.ijhydene.2015.12.145.

[2] An L, Zhao TS. Transport phenomena in alkaline direct ethanol fuel cells for sustainable energy production. J Power Sources 2016;341:199–211. https://doi.org/10.1016/j.jpowsour.2016.11.117.

[3] Fontes EH, Piasentin RM, Ayoub JMS, Da Silva JCM, Assumpção MHMT, Spinacé EV, et al. Electrochemical and in situ ATR-FTIR studies of ethanol electro-oxidation in alkaline medium using PtRh/C electrocatalysts. Mater Renew Sustain Energy 2015;4:3. https://doi.org/10.1007/s40243-015-0043-z.

[4] Antolini E. Catalysts for direct ethanol fuel cells. J Power Sources 2007;170:1–12. https://doi.org/10.1016/j.jpowsour.2007.04.009.

[5] Zhang Z, Xin L, Sun K, Li W. Pd–Ni electrocatalysts for efficient ethanol oxidation reaction in alkaline electrolyte. Int J Hydrogen Energy 2011;36:12686–97. https://doi.org/10.1016/j.ijhydene.2011.06.141.

[6] Beyhan S, Léger JM, Kadırgan F. Understanding the influence of Ni, Co, Rh and Pd addition to PtSn/C catalyst for the oxidation of ethanol by in situ Fourier transform infrared spectroscopy. Appl Catal B Environ 2014;144:66–74. https://doi.org/10.1016/j.apcatb.2013.07.020.

[7] Ma Y, Wang H, Ji S, Linkov V, Wang R. PtSn/C catalysts for ethanol oxidation: the effect of stabilizers on the morphology and particle distribution. J Power Sources 2014;247:142–50. https://doi.org/10.1016/j.jpowsour.2013.08.086.

[8] Maksic A, Smiljanic M, Miljanic S, Rakocevic Z, Strbac S. Ethanol oxidation on Rh/Pd(poly) in alkaline solution. Electrochim Acta 2016;209:323–31. https://doi.org/10.1016/j.electacta.2016.05.096.

[9] Jurzinsky T, Kintzel B, Bär R, Cremers C, Tübke J. Methanol oxidation on PdRh/C electrocatalyst in alkaline media: temperature and methanol concentration dependencies. J Electroanal Chem 2016;776:49–52. https://doi.org/10.1016/j.jelechem.2016.06.038.

[10] Geraldes AN, Furtunato Da Silva D, Martins da Silva JC, Antônio de Sá O, Spinacé EV, Neto AO, et al. Palladium and palladium–tin supported on multi wall carbon nanotubes or carbon for alkaline direct ethanol fuel cell. J Power Sources 2015;275:189–99. https://doi.org/10.1016/j.jpowsour.2014.11.024.

[11] Silva S, Assumpção MHMT, Martins da Silva JC, De Souza RFB, Spinacé EV, Neto AO, et al. PdSn/C electrocatalysts with different atomic ratios for ethanol electro-oxidation in alkaline media. Int J Electrochem Sci 2014;9:5416–24. www.electrochemsci.org/papers/vol9/91005416.pdf.

[12] Bokobza L, Bruneel JL, Couzi M. Raman spectra of carbon-based materials (from graphite to carbon black) and of some silicone composites. J Carbon Res 2015;1:77–94. https://doi.org/10.3390/c1010077.

[13] Moulder J, Stickle WF, Sobol PE, Bomben KD. Handbook of X-ray photoelectron spectroscopy: a reference book of standard spectra for identification and interpretation of XPS data. Minnesota: Physical Electronics Division, Perkin-Elmer Corporation; 1992.

[14] Hofmann S. Auger- and X-ray photoelectron spectroscopy in materials science: a user-oriented guide. 1st ed. Heidelberg: Springer Berlin Heidelberg; 2013.

[15] Baird RJ, Graham GW, Weber WH. $PdRhO_2$ formation during the air oxidation of a Pd-15Rh alloy. Oxid Met 1988;29:435–43. https://doi.org/10.1007/BF00666844.

[16] Doniach S, Sunjic M. Many-electron singularity in X-ray photoemission and X-ray line spectra from metals. J Phys C Solid State Phys 1970;3:285. https://doi.org/10.1088/0022-3719/3/2/010.

[17] Assumpção MHMT, Piasentin RM, Hammer P, De Souza RFB, Buzzo GS, Santos MC, et al. Oxidation of ammonia using PtRh/C electrocatalysts: fuel cell and electrochemical evaluation. Appl Catal B Environ 2015;174(175):136–44. https://doi.org/10.1016/j.apcatb.2015.02.021.

[18] Fierro JLG, Palacios JM, Tomas F. An analytical SEM and XPS study of platinum–rhodium gauzes used in high pressure

ammonia burners. Surf Interface Anal 1988;13:25–32. https://doi.org/10.1002/sia.740130107.
[19] Abe Y, Kato K, Kawamura M, Sasaki K. Rhodium and rhodium oxide thin films characterized by XPS. Surf Sci Spectra 2001;8:117–25. https://doi.org/10.1116/11.20010801.
[20] Newbury DE, Ritchie NWM. Performing elemental microanalysis with high accuracy and high precision by scanning electron microscopy/silicon drift detector energy-dispersive X-ray spectrometry (SEM/SDD-EDS). J Mater Sci 2014;50:493–518. https://doi.org/10.1007/s10853-014-8685-2.
[21] XPS/ESCA, https://www.phi.com/surface-analysis-techniques/xps-esca.html. [acessed 13 october 2018].
[22] Buzzo GS, Orlandi MJB, Teixeira-Neto E, Homem-de-Mello P, Lopes ACG, Franco-Junior E, et al. Effects of catalyst load in Pt and Pb-based catalysts using formic acid oxidation as a model. J Power Sources 2011;199:75–84. https://doi.org/10.1016/j.jpowsour.2011.10.044.
[23] Da Silva SG, Fontes EH, Assumpção MHMT, Linardi M, Spinacé E, César M, et al. Fuel cell and electrochemical studies of the ethanol electro-oxidation in alkaline media using PtAuIr/C as anodes. Ionics 2017;23:2367–76. https://doi.org/10.1007/s11581-017-2088-8.
[24] Moraes LPR, Mato BR, Radtke C, Santiago EI, Fonseca FC, Amico SC, et al. Synthesis and performance of palladium-based electrocatalysts in alkaline direct ethanol fuel cell. Int J Hydrogen Energy 2016;41:6457–68. https://doi.org/10.1016/j.ijhydene.2016.02.150.
[25] Xiao-Zi Yuan JZ, Wang Haijiang. PEM fuel cell electrocatalysts and catalyst layers fundamentals and applications. 1st ed. London: Springer-Verlag London; 2008.
[26] Weber WH, Baird RJ, Graham GW. Raman investigation of palladium oxide, rhodium sesquioxide and palladium. J Raman Spectrosc 1988;19:239–44. https://doi.org/10.1002/jrs.1250190404.
[27] Belka R, Suchanska M, Czerwosz E, Keczkowska J. Raman studies of Pd-C nanocomposites. Open Phys 2013;11:245–50. https://doi.org/10.2478/s11534-012-0138-4.
[28] Holade Y, Canaff C, Poulin S, Napporn TW, Servat K, Kokoh KB. High impact of the reducing agent on palladium nanomaterials: new insights from X-ray photoelectron spectroscopy and oxygen reduction reaction. RSC Adv 2016;6:12627–37. https://doi.org/10.1039/C5RA24829A.
[29] Kim KS, Gossmann AF, Winograd N. X-ray photoelectron spectroscopic studies of palladium oxides and the palladium-oxygen electrode. Anal Chem 1974;46:197–200. https://doi.org/10.1021/ac60338a037.
[30] Hoare JP. The effect of metal dissolution on the rest potential in the palladium-oxygen-acid system. J Electrochem Soc 1964;111:610–5. https://doi.org/10.1149/1.2426193.
[31] Morgan WE, Van Wazer JR. Binding energy shifts in the x-ray photoelectron spectra of a series of related group IVa compounds. J Phys Chem 1973;77:964–9. https://doi.org/10.1021/j100626a023.
[32] Di Giulio M, Serra A, Tepore A, Rella R, Siciliano P, Mirenghi L. Influence of the deposition parameters on the physical properties of tin oxide thin films. Mater Sci Forum 1996;203:143–8. https://doi.org/10.4028/www.scientific.net/MSF.203.143.
[33] Lazzarini A, Piovano A, Pellegrini R, Leofanti G, Agostini G, Rudic S, et al. A comprehensive approach to investigate the structural and surface properties of activated carbons and related Pd-based catalysts. Catal Sci Technol 2016;6:4910–22. https://doi.org/10.1039/C6CY00159A.
[34] Watts JF. High resolution XPS of organic polymers: the Scienta ESCA 300 database. G. Beamson and D. Briggs. Chichester: John Wiley and Sons; 1992. https://doi.org/10.1002/sia.740200310. 280pp., £65. ISBN 0471 935921. Surf. Interface Analysis 1993; 20:267–267.
[35] Lascovich JC, Giorgi R, Scaglione S. Evaluation of the sp2/sp3 ratio in amorphous carbon structure by XPS and XAES. Appl Surf Sci 1991;47:17–21. https://doi.org/10.1016/0169-4332(91)90098-5.
[36] Wagner CD, Davis LE, Zeller MV, Taylor JA, Raymond RH, Gale LH. Empirical atomic sensitivity factors for quantitative analysis by electron spectroscopy for chemical analysis. Surf Interface Anal 1981;3:211–25. https://doi.org/10.1002/sia.740030506.
[37] Scofield JH. Theoretical photoionization cross sections from 1 to 1500 kev. Report, Research Org. California Univ. Livermore. Lawrence Livermore Lab; 1973. https://doi.org/10.2172/4545040.
[38] Geraldes AN, Furtunato DS, Pino ES, Martins da Silva JC, Souza RFB, Hammer P, et al. Ethanol electro-oxidation in an alkaline medium using Pd/C, Au/C and PdAu/C electrocatalysts prepared by electron beam irradiation. Electrochim Acta 2013;111:455–65. https://doi.org/10.1016/j.electacta.2013.08.021.
[39] Palma L M d. Desenvolvimento de células a combustível de álcoois direta: produção de protótipos de alta potência. Ribeirão Preto/SP. Universidade de São Paulo; 2014.
[40] Fontes EH, da Silva SG, Spinacé E, Neto AO, de Souza RFB. In situ ATR-FTIR studies of ethanol electro-oxidation in alkaline medium on PtRh/C electrocatalyst prepared by an alcohol reduction process. Electrocatalysis 2016;7:297–304. https://doi.org/10.1007/s12678-016-0308-z.
[41] Mao H, Wang L, Zhu P, Xu Q, Li Q. Carbon-supported PdSn–SnO_2 catalyst for ethanol electro-oxidation in alkaline media. Int J Hydrogen Energy 2014;39:17583–8. https://doi.org/10.1016/j.ijhydene.2014.08.079.
[42] Dias RR. Preparação e caracterização de eletrocatalisadores PtRu, PtSn, PtRh, PtRuRh e PtSnRh para oxidação direta de álcoois em células a combustível tipo PEM utilizando a metodologia da redução por álcool. São Paulo/SP. Universidade de São Paulo; 2009.
[43] ADVC: free software for the determination of the real surface area of solid electrodes, http://www2.feg.unesp.br/#!/paginas-pessoais/fisica-e-quimica/prof-eduardo-goncalves-ciapina/english-version/software-for-the-determination-of-real-surface-areas-of-solid-electrodes/ [Accessed 13 October 2018].
[44] Souza FM, Nandenha J, Batista BL, Oliveira VHA, Pinheiro VS, Parreira LS, et al. PdxNby electrocatalysts for DEFC in alkaline medium: stability, selectivity and mechanism for EOR. Int J Hydrogen Energy 2018;43:4505–16. https://doi.org/10.1016/j.ijhydene.2018.01.058.